Available online at www.sciencedirect.com
SCIENCE DIRECT®
Earth and Planetary Science Letters xx (2004) xxx–xxx
EPSL
www.elsevier.com/locate/epsl

The effect of temperature on the seismic anisotropy of the perovskite and post-perovskite polymorphs of $MgSiO_3$

Stephen Stackhouse[a,*], John P. Brodholt[a], J. Wookey[b], J.-M. Kendall[b], G. David Price[a]

[a]*Department of Earth Sciences, University College London, Gower Street, London WC1E 6BT, UK*
[b]*School of Earth Sciences, University of Leeds, Leeds, LS2 9JT, UK*

Received 8 August 2004; received in revised form 25 October 2004; accepted 23 November 2004
Editor: B. Wood

Abstract

Using elastic constants determined by ab initio molecular dynamics over a range of temperatures, we show that the seismic anisotropy of $MgSiO_3$ perovskite is significantly temperature dependent. At 90 GPa, the direction of greatest shear wave splitting changes from [001] at 0 K to [010] at 3500 K. In addition, there is no shear wave splitting in the [100] direction at 0 K, but a significant amount of splitting is exhibited at 3500 K. We have also calculated the first set of high-temperature elastic constants of the new post-perovskite phase by ab initio molecular dynamics methods. We find that, in contrast to $MgSiO_3$ perovskite, temperature has little effect on the acoustic anisotropy of this phase. We determine $\partial \ln V_S / \partial \ln V_P$ for the post-perovskite phase and find it to be very low, about 0.9. This may be an important parameter for mapping out the post-perovskite phase in the lowermost mantle.

Keywords: ab initio; molecular dynamics; core–mantle boundary; post-perovskite; high-temperature elasticity; seismic anisotropy

1. Introduction

The core–mantle boundary (CMB) is overlain by a layer that is distinct from the mantle above. This layer, known simply as D″, is only a few hundred kilometres thick, and is thought to act as a thermal and/or compositional boundary separating the predominantly silicate/oxide solid lower mantle from the hotter molten iron outer core. It is also postulated to be the source of plumes and hotspots [1] and perhaps also a graveyard for subducted plates [2].

Seismological investigations of the D″ region show considerable lateral variation in elastic velocity structure, but several prevalent features are distinguishable. In places, the top of the layer is bound by a seismic discontinuity [3,4]. There is

* Corresponding author. Tel.: +44 20 7679 3424; fax: +44 20 7679 2685.
E-mail address: s.stackhouse@ucl.ac.uk (S. Stackhouse).

0012-821X/$ - see front matter © 2004 Elsevier B.V. All rights reserved.
doi:10.1016/j.epsl.2004.11.021

also growing evidence that thin (5–40 km) ultra-low-velocity zones lie at the base of D″ in some regions [5,6]. In addition, shear-wave splitting has been observed in the lower-most part of the mantle [7]. In the circum-Pacific region horizontally polarised shear waves are observed to travel faster than vertically polarised ones by an average of about 1%, while in the central-Pacific area rapid spatial variations are seen. In some regions of the central-Pacific, horizontally polarised waves travel faster than vertically polarised ones, in other areas the opposite is true, and in some places no shear-wave splitting is observed. For further details, see recent reviews [8–12].

These unusual seismic observations may be explained in terms of the crystalline alignment of seismically anisotropic minerals (lattice-preferred orientation (LPO)), which is proposed to develop via dislocation creep, induced by convective flow along the CMB and in upwellings [7,8,10,13]. Other possible theories include the development of orientated melt inclusions (generating shape-preferred orientation (SPO)), and the formation of periodic thin layering (PTL) of minerals with different elastic properties [10,14]. In order to be able to interpret seismic observations in terms of such mechanisms it is essential to know the minerals present and their elastic properties. This poses a problem, since it is still not routine to perform experiments at the high temperature and pressures associated with the CMB. Calculation of elastic properties and seismic anisotropy of potential mineral phases via theoretical mineral physics is therefore invaluable.

The elastic and seismic properties of mineral crystals may be determined from ab initio methods, which solve, to a good approximation, Schrödinger's equation to model interactions in a system of nuclei and electrons. Of these, density functional theory (DFT) [15–17] is one of the most reliable and most efficient methods. The method is able to calculate the equilibrium single crystal structure of mantle minerals and also the stresses induced in them by a given strain, enabling the determination of elastic constants. The literature shows that many mantle minerals have been successfully studied using DFT-based simulation methods [18–35,37–40].

The most common method for structure optimisation using density functional theory is athermal geometry optimisation [18–27]. This neglects thermal effects, such as zero-point motion and lattice-vibrations, which can result in non-insignificant effects on unit cell volumes and elastic constants. Some authors have therefore attempted to correct for thermal effects using an approximation based on the Mie-Grüneisen equation of state [28,29]. More recently, density functional theory-based methods explicitly incorporating thermal effects have been applied to mantle minerals. These encompass lattice-dynamics [30,31] and finite-temperature molecular dynamics [32]. Such methods show that elastic and seismic properties of minerals vary significantly with both pressure and temperature.

The temperature of the core–mantle boundary region ranges from approximately 2800 K up to 4000 K (the temperature of the outer core at the CMB). It is therefore clear that in order to accurately interpret the observed seismic anisotropy it is necessary to know the elastic and seismic properties of mantle minerals at the relevant temperatures and pressures, and not only at the correct pressures (and 0 K), which are commonly calculated. This is illustrated in the present calculations for $MgSiO_3$ perovskite, where temperature is shown to have a very significant effect on the magnitude of acoustic anisotropy. The effect of temperature on the acoustic properties of the newly discovered post-perovskite phase [36–38] is also thoroughly investigated and compared with those determined from high-pressure athermal calculations [39,40].

2. Method

In order to calculate the nine independent elastic constants of the post-perovskite phase, molecular dynamics simulations were performed within the canonical ensemble (NVT), using the projector-augmented-wave implementation [41,42] of the density functional theory-based VASP code [43,44]. This utilises a plane-wave basis set, periodic boundary conditions, and **k**-point sampling. The time-step used in the molecular dynamics simulations was 1 fs. The exchange-correlation functional used adhered to the PW91 form of the generalised gradient approximation [45,46]. The large size of the

cell meant Brillouin zone sampling was restricted to the Γ-point. For a general overview of density functional theory-based simulations, the reader is referred to Payne et al. [47].

Preliminary tests were performed to determine a suitable kinetic energy cut-off for the plane-wave expansion during the molecular dynamics simulation. First, a 20-atom unit cell was constructed from the atomic coordinates and cell parameters published by Murakami et al. [36]. This was optimised at a simulated pressure of 120 GPa, with the Brillioun zone sampled using Monkhort–Pack grids [48] of gradually increasing density (up to a maximum of 8×8×8) and increasing cut-off (up to a maximum of 600 eV). Elastic constants were determined at each level of accuracy by calculating the stresses induced by making three different orthorhombic and one triclinic type strains, of magnitude ±0.3%, ±0.7%, and ±1.0%, to the equilibrium models. It was found that using a Monkhort–Pack grid denser than 6×6×6 and a cut-off larger than 600 eV caused an average of only 0.3% change in the absolute values of the nine calculated elastic constants, which were considered converged.

Next, a much larger post-perovskite simulation cell (60 atoms) was constructed, identical to that which would be used in subsequent molecular dynamics simulations. This was optimised at a simulated pressure of 120 GPa with an increasingly large cut-off. Due to the large size of the cell, only the Γ-point was considered, as would be the case for the molecular dynamics simulations. To make a fair error assessment, elastic constants were calculated for each cut-off value from ±1.0% strains only, as this would be the case for the finite temperature calculations, due to the large computational cost of molecular dynamics. It was found that using a cut-off of 500 eV, elastic constants were obtained that differed by an average of 1.0% from those determined with the small model using a 6×6×6 Monkhort–Pack grid and cut-off of 600 eV, which was considered acceptable, as well as being computationally tractable.

Finite temperature molecular dynamics simulations were therefore performed on the larger post-perovskite model, as is described above, using a cut-off of 500 eV, for a simulated pressure of approximately 136 GPa (corresponding to a depth of 2890 km, commensurate with the bottom of the D″ layer) and temperatures of 3000 K and 4000 K. The equilibrium structures were obtained from 2 ps simulations. Three different orthorhombic and one triclinic type strains of magnitude ±1.0% were applied to the equilibrium structures and the induced stresses were calculated as the average of a 1 ps simulation. In each case the final atomic velocities of the equilibrium simulation were used as initial velocities for the strained model. In this way the model equilibrated extremely quickly. Equilibration was verified by running a longer molecular dynamics simulation of 4 ps—specifically that of post-perovskite at 135 GPa and 4000 K. This showed that the standard deviation in the average values of the stresses calculated over the first, second, third, and fourth picoseconds was, on average, only 0.5 GPa.

The finite temperature elastic constants for $MgSiO_3$ perovskite discussed in this paper were taken from our previous studies [32,33]. These were calculated using an almost identical method, at a simulated pressure of approximately 90 GPa (corresponding to a depth of 2070 km, commensurate with the mid lower mantle) and temperatures of 1500 K and 3500 K. The bulk and shear moduli determined from these studies were later shown to be in good agreement with those calculated from molecular dynamics simulations of much larger models (>1000 atoms) using a non-empirical variation-induced breathing potential [49]. This implies that the size of simulation cell used in our previous studies (80 atoms) [32,33] and that of similar size used in the present study (60 atoms) lead to valid results.

The single-crystal compressional and shear wave velocities for both $MgSiO_3$ perovskite and the post-perovskite phase were calculated from their corresponding elastic constants by solving the Christoffel matrix [50–52]. Single-crystal elasticities are converted to transversely isotropic symmetries using the method outlined by Wentzcovitch et al. [20] where the symmetry axis is assumed to be one of the crystallographic axes.

3. Results

Table 1 lists our elastic constants for $MgSiO_3$ perovskite calculated previously by Oganov et al.,

Table 1
Calculated elastic moduli of $MgSiO_3$ perovskite (GPa), at selected pressures and temperatures

P/GPa	T/K	C_{11}	C_{22}	C_{33}	C_{12}	C_{13}	C_{23}	C_{44}	C_{55}	C_{66}	K	G
90	0	851	1044	995	449	360	385	351	272	293	583	294
88	1500	826	991	945	477	362	396	336	266	264	579	270
88	3500	783	878	850	431	356	395	270	234	195	543	227

Taken from Oganov et al. [32,33].

using finite-temperature molecular dynamics [32,33], with corresponding unit cell parameters, volumes, and densities given in Table 2. The average percentage difference between the elastic constants calculated at 0 K and those determined at 3500 K is about 14%. Of course, a general decrease in their values is expected. If this were a systematic decrease, then using elastic constants from 0 K calculations to predict the relative change in wave velocities with propagation direction would be reasonable, but this is not the case for perovskite. Temperature affects some elastic constants by a few percent (C_{13}) and others (C_{66}) by up to 40%. This gives an indication of the magnitude of errors that are incurred in seismic velocities calculated when neglecting to consider the effect of temperature.

The compressional and shear wave velocities associated with the elastic constants calculated for perovskite are shown in Figs. 1 and 2. These show that for $MgSiO_3$ perovskite, at a pressure of approximately 90 GPa, temperature significantly effects seismic wave velocities. For compressional wave velocities there is an expected decrease in magnitude with temperature, while the dependence on propagation direction remains unaffected. For shear wave velocities, however, there is a pronounced change in dependence on propagation direction in addition to the expected decrease in magnitude. This is seen clearly in Table 3 where shear wave splitting is tabulated for selected propagation directions under various different pressures and temperatures. It can be seen that the direction of greatest shear wave splitting is [001] at 90 GPa and 0 K, but [010] at 88 GPa and 3500 K. In addition, whereas there is almost no shear wave splitting in the [100] direction at 90 GPa and 0 K, a significant amount is seen at 88 GPa and 3500 K.

Table 2
Calculated unit cell parameters of $MgSiO_3$ perovskite at selected pressures and temperatures

P/Gpa	T/K	a/Å	b/Å	c/Å	V/Å^3	ρ/kg m^{-3}
90	0	–	–	–	130.60	5106
88	1500	4.435	4.655	6.420	132.55	5031
88	3500	4.499	4.674	6.492	136.48	4886

Taken from Oganov et al. [32,33].

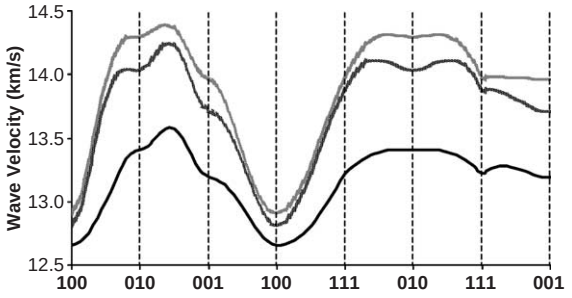

Fig. 1. Variation of compressional wave velocities of $MgSiO_3$ perovskite with propagation direction at approximately 90 GPa and 0 K—light grey, 1500 K—dark grey, and 3500 K—black.

The elastic constants calculated for the recently discovered post-perovskite phase at 136 GPa and various temperatures are listed in Table 4, with associated unit cell parameters, volumes, and densities presented in Table 5. Elastic constants determined at 0 K and 120 GPa are also presented alongside values calculated from previous studies for comparison. There is, in general, excellent agreement between the elastic constants calculated in this study and those determined by Oganov and Ono [37], Tsuchiya et al. [39], and Iitaka et al. [40] and also, as a direct result,

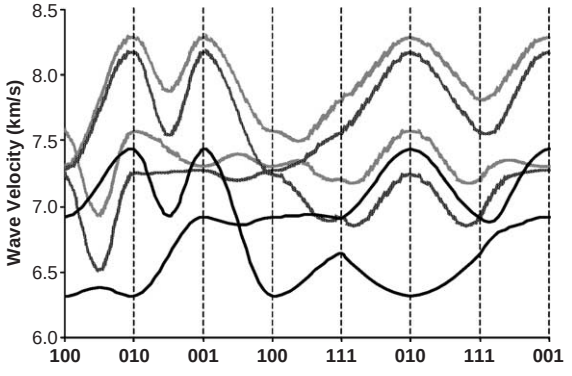

Fig. 2. Variation of shear wave velocities of $MgSiO_3$ perovskite with propagation direction at approximately 90 GPa and 0 K—light grey, 1500 K—dark grey, and 3500 K—black.

Table 3
Shear wave splitting $((V_{S1}-V_{S2})/<V_S>)*100$ for $MgSiO_3$ perovskite in various propagation directions at various pressure and temperatures[a]

P/GPa	T/K	100	010	001	110	111
90	0	3.6	9.4	13.1	11.4	7.9
88	1500	0.4	12.7	12.3	16.7	8.8
88	3500	8.9	16.4	7.5	11.8	3.9

[a] V_{S1} is taken to be the faster than V_{S2} in each case.

between predicted seismic anisotropy. If we now consider only our own results, it can be seen that the average percentage difference between the elastic constants calculated at 0 K and those determined at 4000 K is approximately 16 percent. In contrast to the perovskite case, however, this is always a decrease in magnitude and the range in the percentage decrease is a lot smaller, going from 7% to 23%. This is reflected in the change in calculated wave velocities with temperature.

The compressional and shear wave velocities associated with these values are shown in Figs. 3 and 4. It can be seen that, in contrast to $MgSiO_3$ perovskite, temperature has very little effect on seismic wave velocities of the post-perovskite phase, other than the expected general decrease with temperature. The [100] direction exhibits the greatest degree of shear wave splitting under all conditions, observed in Table 6. This suggests that relative changes in wave velocities with propagation direction may sometimes be correctly determined from 0 K calculations, but as the results for perovskite illustrate this is not always the case and one does not know without checking. The anomalously large shear wave splitting in the post-perovskite phase is independent of temperature, and greater than that calculated for $MgSiO_3$ perovskite.

Table 5
Calculated unit cell parameters of post-perovskite at selected pressures and temperatures

P/GPa	T/K	a/Å	b/Å	c/Å	V/Å^3	ρ/kg m^{-3}
136	0	2.458	8.041	6.103	120.62	5528
136	3000	2.500	8.118	6.157	124.96	5336
135	4000	2.508	8.175	6.180	126.71	5262

There is some evidence that the core–mantle boundary is transversely isotropic in regions [53]. This results from deformation along a glide plane, but with no preferred slip direction. For this reason it is also useful to examine the seismic anisotropy of transversely isotropic aggregates of $MgSiO_3$ perovskite and post-perovskite phase, shown in Figs. 5 and 6. These show the seismic anisotropy for transversely isotropic aggregates of the two mineral phases with symmetry axis along [100], [010], and [001]. In the case of compressional waves, this corresponds to the percentage difference in their velocity as they travel through or perpendicular to the plane. In the case of shear waves, it corresponds to the percentage difference in velocity of horizontally and vertically polarised waves travelling through the plane. Note that a positive value infers that the horizontally polarised

Table 4
Calculated elastic moduli of post-perovskite phase (GPa), at selected pressures and temperatures

	P/GPa	T/K	C_{11}	C_{22}	C_{33}	C_{12}	C_{13}	C_{23}	C_{44}	C_{55}	C_{66}	K	G
[a]	120	0	1252	929	1233	414	326	478	277	266	408	647	328
[b]	120	0	1308	968	1298	444	343	507	295	278	439	681	344
[c]	120	0	1270	937	1264	425	329	493	291	264	412	660	332
[d]	120	0	1258	936	1235	414	328	479	277	261	407	650	327
[e]	120	0	1275	931	1242	416	315	480	279	258	408	650	328
[d]	136	0	1332	995	1318	461	362	525	291	279	442	702	345
[f]	136	3000	1198	909	1183	400	347	500	273	230	360	640	300
[f]	135	4000	1107	847	1131	429	318	441	251	221	361	604	285

[a] Taken from Oganov and Ono [37]—20-atom cell, 6×6×4 Monkhort–Pack grid and 500 eV cut-off.
[b] Taken from Tsuchiya et al. [39]—20-atom cell, 4×4×2 Monkhort–Pack grid and 950 eV cut-off.
[c] Taken from Iitaki et al. [40]—20-atom cell, 8×2×4 Monkhort–Pack grid and 800 eV cut-off.
[d] This work-static optimisation using 20-atom cell, 6×6×6 Monkhort–Pack grid and 600 eV cut-off.
[e] This work-static optimisation using 60-atom cell, only Γ-point considered and 500 eV cut-off.
[f] This work-molecular dynamics using 60-atom cell, only Γ-point considered and 500 eV cut-off.

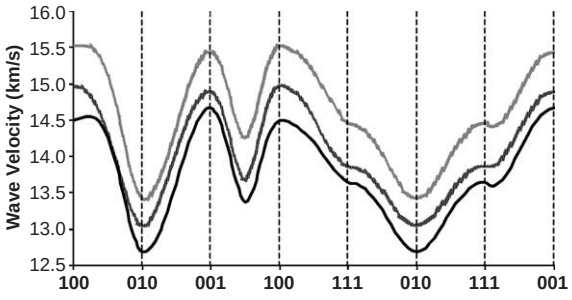

Fig. 3. Variation of compressional wave velocities of post-perovskite phase with propagation direction at approximately 136 GPa and 0 K—light grey, 3000 K—dark grey, and 4000 K—black.

wave travels faster than that vertically polarised and vice versa.

One can see that the calculated transverse anisotropy of $MgSiO_3$ perovskite is greatly affected by temperature. In particular the shear wave splitting for a transversely isotropic aggregate with a symmetry axis in the [010] plane is relatively large at 0 K, while at 3500 K it has almost completely diminished. In addition, shear wave splitting for a transversely isotropic aggregate with a symmetry axis in the [001] plane increases quite significantly with temperature. The effect of temperature on transverse anisotropy is much less pronounced in the case of post-perovskite. The most significant is the decrease in shear wave splitting for a transversely isotropic aggregate with a symmetry axis in the [100] plane at 3000 K. Similar to azimuthal anisotropy, transverse

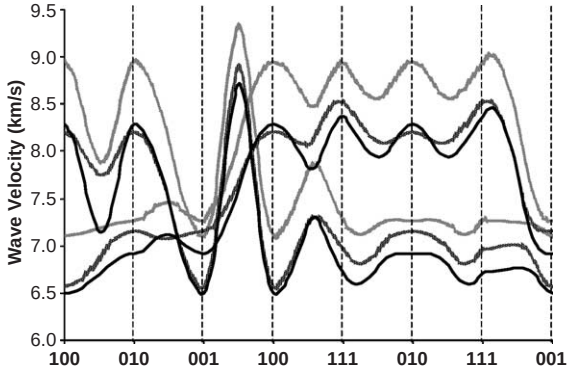

Fig. 4. Variation of shear wave velocities of post-perovskite phase with propagation direction at approximately 136 GPa and 0 K—light grey, 3000 K—dark grey, and 4000 K—black.

Table 6
Shear wave splitting $((V_{S1}-V_{S2})/<V_S>)*100$ for post-perovskite in various propagation directions at various pressure and temperatures[a]

P/GPa	T/K	100	010	001	110	111
136	0	23.2	21.3	2.0	8.8	21.1
136	3000	22.0	14.1	7.9	11.7	21.0
136	4000	24.4	18.7	5.7	6.0	22.6

[a] V_{S1} is taken to be the faster than V_{S2} in each case.

anisotropy is much greater in post-perovskite as compared to $MgSiO_3$ perovskite.

The dependence of bulk and shear modulus on temperature is shown in Fig. 7 and that of the compressional, shear, and bulk velocities is illustrated in Fig. 8. Important derivatives for these are also reported in Tables 7 and 8. The temperature dependence of bulk and shear moduli of both mineral phases are comparable. There are, however, significant differences in the temperature dependence of seismic velocities. For $MgSiO_3$ perovskite, compressional

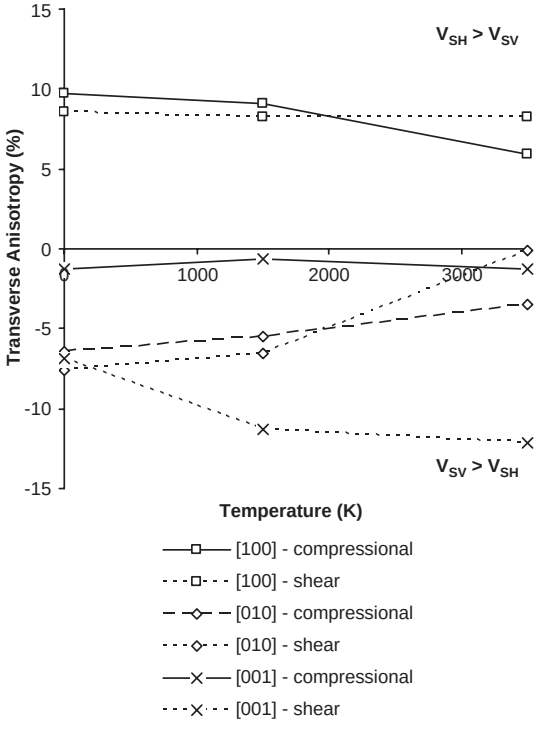

Fig. 5. Temperature dependence of seismic wave velocity anisotropy for a transversely isotropic aggregate of $MgSiO_3$ perovskite phase with symmetry axis along [100], [010], and [001].

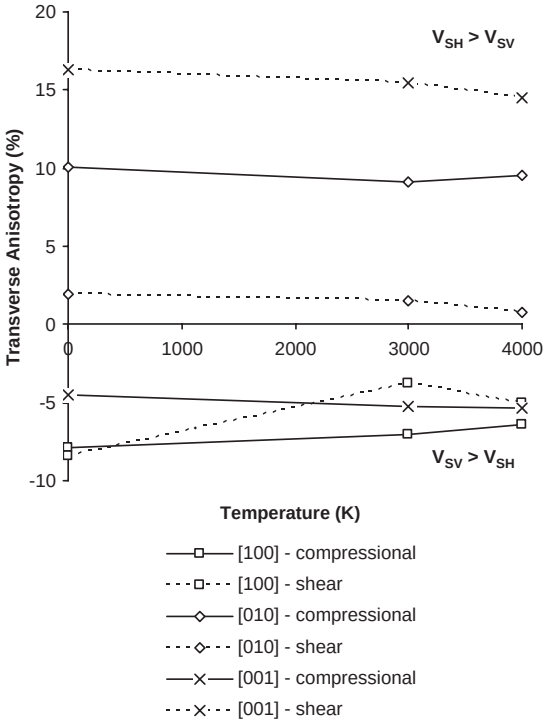

Fig. 6. Temperature dependence of seismic wave velocity anisotropy for a transversely isotropic aggregate of post-perovskite phase with symmetry axis along [100], [010], and [001].

wave velocities decrease approximately half as fast as do shear wave velocities, as the temperature increases, while for post-perovskite they decrease at a similar rate. This leads to an anomalously low $R_{S/P}$ value of 0.9 for post-perovskite, in comparison to 1.9 for perovskite.

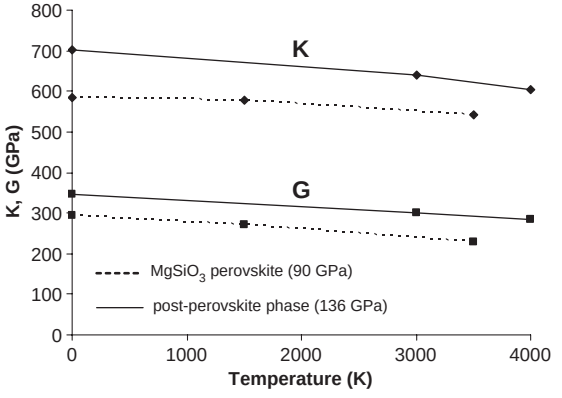

Fig. 7. Temperature dependence of bulk (K) and shear (G) moduli for $MgSiO_3$ perovskite at approximately 90 GPa and post-perovskite phase at approximately 136 GPa. See Table 7 for important derivatives.

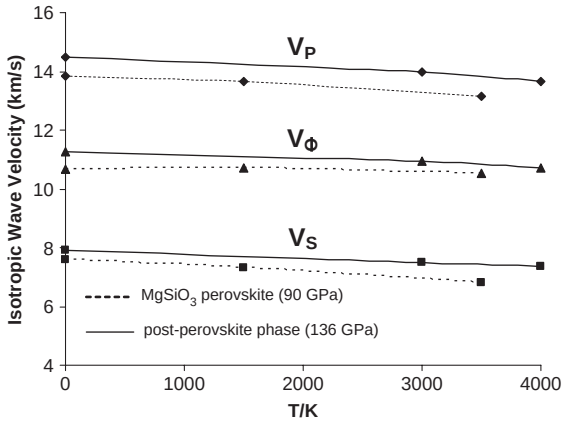

Fig. 8. Temperature dependence of compressional (V_P), shear (V_S), and bulk (V_Φ) isotropic wave velocities for $MgSiO_3$ perovskite at approximately 90 GPa and post-perovskite phase at approximately 136 GPa. See Table 8 for important derivatives.

4. Discussion and conclusions

To assign part, or all, of the observed seismic anisotropy at the core–mantle boundary to a particular mineral, it is necessary to know both the slip systems and seismic anisotropy of the mineral at the relevant temperature and pressure. Although the slip systems of $MgSiO_3$ perovskite and post-perovskite under CMB conditions are not known, we can make simple arguments presuming the relevant slip systems at low pressures are the same as at the conditions of the core–mantle boundary.

For example, assuming the most important slip system in $MgSiO_3$ perovskite is <100> {001}, as implied in a recent study of the mineral at 25 GPa and 1673 K [54], horizontal "mantle-flow" would produce a transversely isotropic aggregate, with a symmetry

Table 7
Temperature dependence of bulk (K) and shear (G) moduli for $MgSiO_3$ perovskite at approximately 90 GPa and post-perovskite phase at approximately 136 GPa

	$(\partial K_T/\partial T)_P/10^{-3}$ (GPa K^{-1})	$(\partial G_T/\partial T)_P/10^{-3}$ (GPa K^{-1})
$MgSiO_3$ perovskite [32]	−21	−18
Post-perovskite phase	−24	−15

Table 8
Temperature dependence of compressional (V_P), shear (V_S), and bulk (V_Φ) isotropic wave velocities for $MgSiO_3$ perovskite at approximately 90 GPa and post-perovskite phase at approximately 136 GPa

	$(\partial \ln V_P/\partial T)_P/10^{-5}$ (km s^{-1} K^{-1})	$(\partial \ln V_S/\partial T)_P/10^{-5}$ (km s^{-1} K^{-1})	$(\partial \ln V_\Phi/\partial T)_P/10^{-5}$ (km s^{-1} K^{-1})	$R_{S/P}=(\partial \ln V_S/\partial \ln V_P)_P$
$MgSiO_3$ perovskite [32]	−1.98	−3.78	−0.92	1.91
Post-perovskite phase	−2.07	−1.87	−2.20	0.90

axis in the [001] direction. Looking at Fig. 5, we see that at 0 K the shear wave transverse anisotropy is −7%, while at 4000 K it is −12%, which is significantly larger. If a transversely isotropic aggregate with a symmetry axis in the [010] was expected, as suggested by Karato et al. [55], the contrast would be, more extreme, with −8% transverse anisotropy at 0 K, but virtually none at 3500 K. Note that neither of these explain the more common observation that horizontally polarised shear waves travel faster than vertically polarised, but rather the opposite. For this to be the case, the slip plane in $MgSiO_3$ perovskite would have to be normal to the [100] axis, as pointed out by Wentzcovitch et al. [20].

In the case of the post-perovskite phase, temperature is calculated to have little effect on transverse anisotropy. Therefore our inference with regard to its slip-planes is the same as that of Tsuchiya et al. [39], made on the basis of athermal results, namely: that for horizontally polarised shear waves to travel faster than vertically polarised shear waves the post-perovskite phase must form a transversely isotropic aggregate with a symmetry axis in the [001] direction. The most probable slip system of post-perovskite is, as yet, unknown under any conditions.

The ratio of lateral variation of compressional to shear wave velocities has been estimated from seismic observations and provides a constraint on the composition of the lower mantle [56,57]. In particular, $R_{S/P}=\partial \ln V_S/\partial \ln V_P$, is shown to increase from a value of about 1.5 up to approximately 2.5, going from a depth of 1000 km down to 2400 km. The calculated value of $R_{S/P}$ for perovskite and the post-perovskite phase are given in Table 6. The calculated value for the post-perovskite phase is remarkably low, about 0.9. This low value comes mainly from the very low $(\partial \ln V_S/\partial T)_P$ value for post-perovskite as compared to perovskite, with their $(\partial \ln V_P/\partial T)_P$ values being very similar. Taken at face value, this low value of $R_{S/P}$ is totally incompatible with that observed and would seem to cast doubt on the existence of the post-perovskite phase in D″. It is quite likely, however, that the proportion of perovskite and post-perovskite varies considerably in D″ and it is not clear how this would be reflected in an average value of $R_{S/P}$, which is what is determined from seismic tomography. We point out, however, that this low value of $R_{S/P}$ for the post-perovskite phase may make it possible to map out regions of post-perovskite in the lowermost mantle.

The effect of iron, thought likely to be present in post-perovskite at lower mantle conditions [58], remains to be investigated.

References

[1] F.D. Stacey, D.E. Loper, The thermal boundary layer interpretation of D″ and its role as a plume source, Phys. Earth Planet Inter. 16 (1983) 45–55.
[2] P.G. Silver, R.W. Carlson, P. Olson, Deep slabs, geochemical heterogeneity, and the large-scale structure of mantle convection: investigation of an enduring paradox, Annu. Rev. Earth Planet. Sci. 16 (1988) 477–541.
[3] M.E. Wysession, T. Lay, J. Revenaugh, Q. Williams, E.J. Garnero, R. Jeanloz, L.H. Kellogg, The D″ discontinuity and its implications, in: M. Gurnis, M.E. Wysession, E. Knittle, B.A. Buffett (Eds.), The Core–Mantle Boundary Region, American Geophysical Union, Washington, 1998.
[4] I. Sidorin, M. Gurnis, D.V. Helmberger, Evidence for a ubiquitous seismic discontinuity at the base of the mantle, Science 286 (1999) 1326–1331.
[5] E.J. Garnero, D.V. Helmberger, A very low basal layer underlying large-scale low-velocity anomalies in the lower mantle beneath the Pacific: evidence from core phases, Phys. Earth Planet Inter. 91 (1995) 161–176.
[6] E.J. Garnero, J. Revenaugh, Q. Williams, T. Lay, L.H. Kellogg, Ultralow velocity zone at the core–mantle boundary, in: M. Gurnis, M.E. Wysession, E. Knittle, B.A. Buffett (Eds.), The Core–Mantle Boundary Region, American Geophysical Union, Washington, 1998.
[7] J.-M. Kendall, P.G. Silver, Investigating causes of D″ anisotropy, in: M. Gurnis, M.E. Wysession, E. Knittle, B.A. Buffett (Eds.), The Core–Mantle Boundary Region, American Geophysical Union, Washington, 1998, pp. 97–118.

[8] S. Karato, Some remarks on the origin of seismic anisotropy in the D″ layer, Earth Planets Space 50 (1998) 1019–1028.
[9] T. Lay, Q. Williams, E.J. Garnero, The core–mantle boundary layer and deep Earth dynamics, Nature 392 (1998) 461–468 (1998).
[10] J.-M. Kendall, Seismic anisotropy in the boundary layers of the mantle, in: S. Karato, A.M. Forte, R.C. Liebermann, G. Masters, L. Stixrude (Eds.), Earth's Deep Interior: Mineral Physics and Tomography From the Atomic to the Global Scale, American Geophysical Union, Washington, 2000.
[11] E.J. Garnero, T. Lay, D″ shear velocity heterogeneity, anisotropy and discontinuity structure beneath the Caribbean and Central America, Phys. Earth Planet Inter. 140 (2003) 219–242.
[12] M. Panning, B. Romanowicz, Inferences on flow at the base of Earth's mantle based on seismic anisotropy, Science 303 (2004) 351–353.
[13] A.K. McNamara, S.-H. Karato, P.E. van Keken, Localization of dislocation creep in the lower mantle: implications for the origin of seismic anisotropy, Earth Planet. Sci. Lett. 191 (2001) 85–99.
[14] J.-M. Kendall, P.G. Silver, Constraints from seismic anisotropy on the nature of the lowermost mantle, Nature 381 (1996) 409–412.
[15] P. Hohenberg, W. Kohn, Inhomogeneous electron gas, Phys. Rev. 136 (1964) B864–B871.
[16] W. Kohn, L.J. Sham, Self-consistent equations including exchange and correlation effects, Phys. Rev. 140 (1965) A1133–A1138.
[17] R.G. Parr, W. Yang, Density-functional theory of atoms and molecules, Oxford University Press, Oxford, 1989.
[18] B.B. Karki, L. Stixrude, S.J. Clark, M.C. Warren, G.J. Ackland, J. Crain, Structure and elasticity of MgO at high pressure, Am. Mineral. 82 (1997) 51–60.
[19] B.B. Karki, M.C. Warren, L. Stixrude, G.J. Ackland, J. Crain, Ab initio studies of high-pressure structural transformations in silica, Phys. Rev., B 55 (1997) 3465–3471.
[20] R.M. Wentzcovitch, B.B. Karki, S. Karoto, C.R.S. Da Silva, High pressure elastic anisotropy of $MgSiO_3$ perovskite and geophysical implications, Earth Planet. Sci. Lett. 164 (1998) 371–378.
[21] B. Holm, R. Ahuja, Ab initio calculation of elastic constants of SiO_2 stishovite and α-quartz, J. Chem. Phys. 111 (1999) 2071–2074.
[22] J.P. Brodholt, Pressure-induced changes in the compression mechanism of aluminous perovskite in the Earth's mantle, Nature 407 (2000) 620–622.
[23] B. Kiefer, L. Stixrude, R.M. Wentzcovitch, Elasticity of (Mg, Fe)SiO_3-perovskite at high pressures, Geophys. Res. Lett. 29 (2002) 14683.
[24] R.M. Wentzcovitch, J.L. Martins, G.D. Price, Ab initio molecular dynamics with variable cell shape: application to $MgSiO_3$, Phys. Rev. Lett. 70 (1993) 3947–3950.
[25] R.M. Wentzcovitch, N.L. Ross, G.D. Price, Ab initio study of $MgSiO_3$ and $CaSiO_3$ perovskites at lower-mantle pressures, Phys. Earth Planet Inter. 90 (1995) 101–112.
[26] L. Stixrude, Elastic constants and anisotropy of $MgSiO_3$ perovskite, periclase, and SiO_2 at high pressure, in: M. Gurnis, M.E. Wysession, E. Knittle, B.A. Buffett (Eds.), The Core–Mantle Boundary Region, American Geophysical Union, Washington, 1998.
[27] W. Duan, B.B. Karki, R.M. Wentzcovitch, High-pressure elasticity of alumina studied by first principles, Am. Mineral. 84 (1999) 1961–1966.
[28] A.R. Oganov, J.P. Brodholt, G.D. Price, Comparative study of quasiharmonic lattice dynamics, molecular dynamics and Debye model applied to $MgSiO_3$ perovskite, Phys. Earth Planet Inter. 122 (2000) 277–288.
[29] B. Kiefer, L. Stixrude, J. Hafner, G. Kresse, Structure of wadsleyite at high pressures, Am. Mineral. 86 (2001) 1387–1395.
[30] B.B. Karki, R.M. Wentzcovitch, S. de Gironcoli, S. Baroni, First-principles determination of elastic anisotropy and wave velocities of MgO at lower mantle conditions, Science 286 (1999) 1705–1707.
[31] R.M. Wentzcovitch, B.B. Karki, M. Cococcioni, S. de Gironcoli, Thermoelastic properties of $MgSiO_3$-perovskite: insights on the nature of the Earth's lower mantle, Phys. Rev. Lett. 92 (2004) 18501.
[32] A.R. Oganov, J.P. Brodholt, G.D. Price, The elastic constants of $MgSiO_3$ perovskite at pressures and temperatures of the Earth's mantle, Nature 411 (2001) 934–937.
[33] A.R. Oganov, J.P. Brodholt, G.D. Price, Ab initio elasticity and thermal equation of state of $MgSiO_3$ perovskite, Earth Planet. Sci. Lett. 184 (2001) 555–560.
[34] J.R. Alvarez, P. Rez, Electronic structure of stishovite, Solid State Commun. 108 (1998) 37–42.
[35] M.D. Teter, J. Hemley, G. Kresse, J. Hafner, High pressure polymorphism in silica, Phys. Rev. Lett. 80 (1998) 2145–2147.
[36] M. Murakami, K. Hirose, K. Kawamura, N. Sata, Y. Ohishi, Post-perovskite phase transition in $MgSiO_3$, Science 304 (2004) 855–858.
[37] A.R. Oganov, S. Ono, Theoretical and experimental evidence for a post-perovskite phase of $MgSiO_3$ in Earth's D″ layer, Nature 430 (2004) 445–448.
[38] T. Tsuchiya, J. Tsuchiya, K. Umemoto, R.M. Wentzcovitch, Phase transition in $MgSiO_3$ perovskite in the earth's lower mantle, Earth Planet. Sci. Lett. 224 (2004) 241–248.
[39] T. Tsuchiya, J. Tsuchiya, K. Umemoto, R.M. Wentzcovitch, Elasticity of post-perovskite $MgSiO_3$, Geophys. Res. Lett. 31 (2004) (art. no. L14603).
[40] T. Iitaka, K. Hirose, K. Kawamura, M. Murakami, The elasticity of the $MgSiO_3$ post-perovskite phase in the Earth's lowermost mantle, Nature 430 (2004) 442–445.
[41] P.E. Blöchl, Projector augmented-wave method, Phys. Rev., B 50 (1994) 17953–17979.
[42] G. Kresse, D. Joubert, From ultrasoft pseudopotentials to the projector augmented-wave method, Phys. Rev., B 59 (1999) 1758–1775.
[43] G. Kresse, J. Furthmüller, Efficient interative schemes for ab initio total-energy calculations using a plane-wave basis set, Phys. Rev., B 54 (1996) 11169–11186.
[44] G. Kresse, J. Furthmüller, Efficiency of ab initio total energy calculations for metals and semiconductors using a plane-wave basis set, Comput. Mater. Sci. 6 (1996) 15–50.

[45] J.P. Perdew, J.A. Chevary, S.H. Vosko, K.A. Jackson, M.R. Pederson, D.J. Singh, C. Fiolhais, Atoms, molecules, solids, and surfaces—applications of the generalized gradient approximation for exchange and correlation, Phys. Rev., B 46 (1992) 6671–6687.

[46] Y. Wang, J.P. Perdew, Correlation hole of the spin-polarized electron-gas, with exact small-wave-vector and high density scaling, Phys. Rev., B 44 (1991) 13 298–13 307.

[47] M.C. Payne, M.P. Teter, D.C. Allan, T.A. Arias, J.D. Joannopoulos, Iterative minimization techniques for ab initio total-energy calculations: molecular dynamics and conjugate gradients, Rev. Mod. Phys. 64 (1992) 1045–1097.

[48] H.J. Monkhorst, J.D. Pack, Special points for Brillouin-zone intergrations, Phys. Rev., B 13 (1976) 5188–5192.

[49] F.C. Marton, R.E. Cohen, Constraints on lower mantle composition from molecular dynamics of $MgSiO_3$ perovskite, Phys. Earth Planet. Inter. 134 (2002) 239–252.

[50] M.J.P. Musgrave, Crystal acoustics, Holden-Day, San Francisco, 1970.

[51] S.P. Cheadle, R.J. Brown, D.C. Lawton, Orthorhombic anisotropy: a physical seismic modelling study, Geophysics 56 (1991) 1603–1613 (1991).

[52] I. Tsvankin, Anisotropic parameters and *p*-wave velocity for orthorhombic media, Geophysics 62 (1997) 1292–1309.

[53] C. Thomas, J.-M. Kendall, The lowermost mantle beneath northern Asia: II. Evidence for lower-mantle anisotropy, Geophys. J. Int. 151 (2002) 296–308.

[54] P. Cordier, T. Ungár, L. Zsoldos, G. Tichy, Dislocation creep in $MgSiO_3$ perovskite at the conditions of the Earth's uppermost mantle, Nature 428 (2004) 837–840.

[55] S. Karato, S. Zhang, H.-R. Wenk, Superplasticity in Earth's lower mantle: evidence from seismic anisotropy and rock physics, Science 270 (1995) 458–461.

[56] G.S. Robertson, J.H. Woodhouse, Constraints on lower mantle physical properties from seismology and mineral physics, Earth Planet. Sci. Lett. 143 (1996) 197–205.

[57] S.I. Karato, B.B. Karki, Origin of lateral variation of seismic wave velocities and density in the deep mantle, J. Geophys. Res. 106 (2001) 21 771–21 783.

[58] W.L. Mao, G. Shen, V.B. Prakapenka, Y. Meng, A.J. Campbell, D.L. Heinz, J. Shu, R.J. Hemley, H.-K. Mao, Ferromagnesian post-perovskite silicates in the D″ layer of the Earth, Proc. Natl. Acad. Sci. 101 (2004) 15867–15869.